Kirigami-based compliant mechanism for multi-axis optical tracking and energy-harvesting applications

*Erin E. Evke[1], Chao Huang[1], Yu-Wei Wu[1], Michael Arwashan,[2], Byungjun Lee[3], Stephen R. Forrest[1,3], Max Shtein[1]**

[1] Department of Materials Science and Engineering
University of Michigan
Ann Arbor, MI 48105, USA

[2] Department of Mechanical Engineering
University of Michigan
Ann Arbor, MI 48105, USA

[3] Department of Electrical Engineering and Computer Science
University of Michigan
Ann Arbor, MI 48105, USA

* Corresponding author. Email: mshtein@umich.edu

Abstract

Kirigami-based structures and materials have recently emerged with a variety of geometric transformation capabilities in applications such as flexible electronics, soft robotics, nano-photonics, energy-harvesting, and others. This work presents a 2-dimensional pattern of cuts (kirigami) that transforms into a 3-dimensional, one-piece compliant mechanism that allows for optical tracking over a solid angle sweep of over 110˚ in two axes. This structure can be scaled to an arbitrarily large array, yet the displacement required to achieve the angular sweep remains

This is the author manuscript accepted for publication and has undergone full peer review but has not been through the copyediting, typesetting, pagination and proofreading process, which may lead to differences between this version and the Version of Record. Please cite this article as doi: 10.1002/adem.202001079.

compact and independent of the number of elements and areal extent of the array. One of the applications of this mechanism is in solar concentration and dual-axis tracking. Using practical dimensions, 80-fold or greater concentration can be realized. Mutual shadowing of nearby concentrators is assessed along with thermal effects of optical concentration that limit photovoltaic cell efficiency. The significant reduction in semiconductor usage along with the multi-axis tracking ability will reduce the overall cost of solar photovoltaic panels. This is projected to make them competitive with stationary silicon panels capable of satisfying the household daily average energy requirement.

Keywords

Kirigami, tracking, optical, multi-axis, compliant mechanism

1. Introduction

The ancient Japanese arts of *origami* (folding) and *kirigami* (cutting) have provided a versatile conceptual framework for transforming relatively easily manufactured two-dimensional patterns into three-dimensional structures that would be difficult to produce using other approaches.[1-5] Thereby, numerous elegant solutions have been demonstrated to long-standing problems in a variety of fields including soft robotics,[6-8] health monitoring,[9,10] antennas,[11] flexible electronics,[12-14] optical beam steering,[15] photonic applications,[16-20] and solar energy harvesting.[21-23]

Despite steady advances in the efficiency[24,25] of photovoltaic devices, widespread adoption of ultra-high efficiency materials remains limited due to the high cost of high-efficiency semiconductor photovoltaic (PV) cells.[26] Concentrated photovoltaic (CPV) systems reduce semiconductor requirements; however, most designs have a narrow acceptance angle and therefore require precise tracking.[27,28] Conventional trackers used to achieve the required tracking precision are large, heavy, complex, costly, and unsuitable for deployment in many desirable locations

including residential rooftops.[27–29] Thus, a number of recent works have tried to address the limitations of narrow acceptance angle, tracking ability, and cost. Grede and Giebink proposed a concentrator shape that maintains over 90% optical efficiency over 140˚,[30] and microcell arrays have been proposed to reduce concentrator cost and weight.[31,32] Origami and kirigami techniques have also been shown to overcome some limitations of existing trackers, including *miura-ori* and "flasher" origami patterns as deployable solar arrays.[23,33-35] However, many of these patterns require more semiconductor material than conventional panels, are not easily manufacturable due to the intricate folds required, and exhibit poor fatigue performance.

A kirigami-based, low-profile, singe-axis solar tracker was shown recently, incorporating gallium arsenide (GaAs) photovoltaic cells directly on a flexible substrate, laser-cut into a simple linear kirigami pattern that enabled "stretching" the solar cell, while progressively tilting the photovoltaic material toward the sun, over the course of the day without damage.[21] This approach achieved a 36% reduction in semiconductor needed relative to a stationary device and avoided complex folds and mitigated optical losses due to scattering (e.g. on overcast days). To improve the economy of semiconductor material, another study combined kirigami-based tracking with optical concentration, which achieved a 6-fold optical concentration using non-imaging, folded, or molded optics mated to a kirigami substrate. This enabled diurnal tracking and resulted in a 4.5x overall reduction in the semiconductor required.[36] Here we introduce a kirigami pattern that enables dual-axis tracking, is robust, and easily scaled to large-area arrays, and it can be integrated with a variety of optical elements. As proof of concept, we explore its utility for a solar tracking mini-CPV application that dramatically reduces the amount of semiconductor material required.

2. Results and Discussion

Kirigami design, fabrication, and testing of the compliant mechanism

The baseline kirigami cut pattern consists of discontinuous concentric hexagonal cuts as shown in the inset of **Figure 1b**; each hexagonal "ring" has two diametrically opposed splits rotated by 90˚

between each concentric set. The hexagonal pattern has an overall three-fold rotational symmetry about the central axis. When a force is applied to the middle of the pattern, the subsequent beams bend out of plane forming a series of concentric rings that alternate between ~~along the C_3 rotational symmetry axis~~ as depicted in **Figure 1a**~~, the 3-fold symmetry is broken~~. The~~is creates~~ S-shaped beams created~~, which~~ are connected *via* saddle-points formed by the uncut regions. In other words, the saddle-points refer to the points at the ends of the cuts. Their influence on the maximum achievable tilt angle will be discussed further later. This provides structural continuity between the outer- and inner-most hexagons. In the expanded structure, these become the "top"- and "bottom"-most horizontal members. When sliding them parallel to each other as depicted in **Figure 1a**, the symmetry is further broken, causing the connecting beams to tilt simultaneously. A close examination of the structure in the side view reveals that previously aligned saddle-points are located on the same cut perimeter in the middle ring. A red line connecting the two saddle points that results in tilt angle, θ, is shown for clarity in **Figure 1a**. The relationship between the angle θ and the lateral displacement, δ, is controlled by the geometry of the cuts and cross-plane displacement, *z*. Also shown in **Figure 1a** is a top-view perspective, where the color bar indicates the normalized Von Mises stress. Finite Element (FE) modeling clearly shows that stress is concentrated in the cut ends, informing the placement of other elements within the structure with minimal risk of structural damage.

The structure described above and shown in **Figure 1** is simple to fabricate using a number of scalable methods; for the purposes of this demonstration, 100 μm thick polyethylene terephthalate (PET) sheets are laser-cut. Tilt angle, θ as a function of δ was measured (**Figure 1b**) showing a monotonic, approximately linear dependence, having an R^2 value of 0.99:

$$\theta = 1.8\delta + 2.9. \quad (1)$$

This dependence is applicable for the cut pattern shown in the inset of **Figure 1b** in which there are two cuts per "ring", *z* = 45 mm, the radial spacing between cuts (*w*) is 1.5 mm, the angular spacing

(φ) formed by the cut ends from the center is 6˚, and the phase shift (γ) referring to the central angle of the placement of the hinges, non-cut regions, with respect to the side is 0˚. Note the slight offset could be attributed to the camera rotation during data collection. Furthermore, the influence of varying cut parameters and directionality of displacement, δ, are discussed and depicted in **Figure S1**. There, it is shown how the simultaneous displacement in the x- and y-direction yields an offset angle. For instance, the substrate when displaced 25 mm at 50˚ translates to 18.7 mm in the *x*-direction (0˚) and 22.3 mm in the *y*-direction (90˚), see **Figure S1i** and **Table S1** for the corresponding displacement coordinates**.**

For a variety of tracking applications, repeated displacement is expected, and it is important to know the force and work required to perform the movement, as well as the fatigue life of the structure. **Figure 1c** shows that to induce tilting, an average of 0.3 mJ are required over a lateral displacement from 0 to 25 mm for *z* = 35 mm. Despite large global deformations, this range of δ is well within the linear elastic regime of the structure (see **Figure S2** for detailed results of shear and uniaxial tests). **Figure 1d** shows the δ behavior as a function of θ incurs no hysteresis in the work required for a cycle after performing 20,000 cycles at a strain rate of 1 mm/s. This indicates there is minimal perceptible plastic deformation of the structure. One cycle is performed to follow the sun throughout the day and another cycle to return to the original position before sunrise the next day. Error bars are included for the control and 2,000 cycle cases; deviations are attributed due to human error in re-aligning the substrate in 3D printed holders attached to tensile grips during shear tests, due to test apparatus limitations.

The individual-concentrator tracker assembly lends itself to creating a low-profile array in which the motion of the individual actuators is intrinsically synchronized. **Figure 1d** shows the top view of hexagonal concentrators arranged in a honeycomb pattern and deformed such that $z = 35\ mm$ at displacements of $\delta = 0\ mm$ and $\delta = 25\ mm$. The side view of a physical array at $\delta = 0\ mm$ and $\delta = 25\ mm$ when $z = 35\ mm$ are also shown in **Figure 1e**. Translating the top (or bottom) plane by 25 mm induces the same maximum tilt angle for each of the concentrators.

That is, the same amount of lateral translation is required independent of array size. In addition, the lightweight hexagonal kirigami pattern requires significantly less work to induce a desired tilt response compared to standard trackers. A major drawback of many mechanical trackers and actuators is the parasitic energy loss due to the use of large mechanical motors, hinged joints, and moving mass required to tilt a photovoltaic panel or optical array.[28] Standard trackers that rely on rotating the entire panel at once require more work and occupy a larger tracking region when increasing the size of the panel. They also often need heavy and bulky supports. For instance, if the kirigami-based tracker panel is 180 m^2, a total of approximately 0.04 kJ would be required to tilt all of the concentrators to 55˚ at z = 35 mm; in contrast, >128 kJ would be required by a 10x18-m rectangular silicon solar panel with a mass density of 15.13 kg/m^2 [37] at a height of 8.2 m at a tilt angle of 55˚.

Consider now the imaginary segment previously highlighted in red in **Figure 1a** connecting two saddle points on a given perimeter of the cuts. To realize a solar tracking, micro-concentrator device, we insert a hexagonal parabolic mirror in this location and adhere it along its outer edge to the kirigami spring. The concentrator is fabricated by vacuum thermoforming a 250 μm polyethylene terephthalate glycol (PETG) sheet at 105˚C for 10 min. This is followed by 0.5 μm of Ag deposited by vacuum thermal evaporation (for details, see **Figure S3**). The front-facing side of the hexagonal paraboloid is then attached to a sheet of transparent material (here PET is used for convenience). The PET sheet has a hole in its center, which is at the focal point of the parabolic mirror. A small photodiode is then aligned in the hole facing down towards the mirror. This assembly is inserted and affixed to the kirigami structure as indicated in **Figure 2a**. Sliding the bottom portion of the kirigami unit cell in a manner depicted in **Figure 2b** produces a tilt of the concentrator-spring assembly in accordance with Equation (1). The neutral position of the kirigami solar tracking system is represented in the left image of **Figure 2b**, where z is the height of the spring, and the cut pattern is represented in the inset of **Figure 2c**; (A) are the pivot points when the innermost ring is laterally displaced in the y-direction, and (B) are the pivot points when displaced

in the *x*-direction. The right-side image in **Figure 2b** shows the structure with deflection δ in the *y*-direction, the outermost hexagonal ring being fixed in place. **Figure 2c** plots the experimentally measured θ vs. δ of the concentrator-spring assembly. The inset of **Figure 2c** shows the cut pattern and directions of δ; the pink shaded region represents the concentrator area. The height of the spring is set at 33 and 45 mm, and the innermost hexagon is displaced in the *x*- and *y*-directions to determine the effects of changing the *z* and directions of δ. The 33 mm height is chosen such that the corner of the concentrator does not contact the base plate at the maximum tilt angle, and also keeps the height of the array reasonably small. A greater height was also tested for comparison. We find that the mechanism performs better when the height of the expanded spring remains smaller than the displacement at which plastic deformation occurs. (The maximum tilt angle as a function of height without concentrators is also depicted in **Figure S1**.) At each specified displacement, an image of the system was taken using a camera, and the tilt angle of the concentrator was determined using Image J. A displacement of δ = 25 mm in the *x*-direction results in a larger maximum tilt angle compared to the same displacement in the *y*-direction. Furthermore, increasing the height of the spring decreases the maximum tilt angle θ_{max} as expected for an equivalent hinged mechanism.

The relationship between displacement and tilt depends on the cut parameters (e.g., radial spacing, phase angle, phase shift, and number of cuts along the perimeter; see **Figure S1**) and is approximately predictable using cantilever beam theory.[9,22,38] When increasing the radial spacing and phase angle, the beams become wider and shorter, respectively, increasing their stiffness. Shortening the length of the beam decreases the distance between the two pivot points, which increases the tilt angle. If the height of the spring is too short, the concentrator will encounter the base that restricts further tilting. The rate of increase in θ vs. δ differs for this system when the concentrator is facing up *versus* down due to gravity (**Figures S4** and **S5**). There is also an accompanying shift, μ, of the concentrator in the δ direction, which increases with δ (**Figure S5**). Through optimization of the cut pattern, sheet thickness, and composition, these phenomena can be controlled and minimized, and greater tilt angles may be achievable.

Figure 3 shows how an individual kirigami-spring concentrator assembly tracks a moving light source using a photodiode in the focal point of the concentrator. The top view of the system is depicted in **Figure 3a**, which shows the kirigami spring, the placement of the concentrator with respect to the spring, and the centered photodiode; a side view is shown in **Figure 3b**. As the light source positioned on a goniometer rotated by θ in one-degree increments, the concentrator matched θ through δ of the innermost hexagon, while the outermost portion of the spring remained fixed. For experimental convenience, the light source faced upward in the laboratory reference frame, and the tracker was positioned such that the concentrator faced the light source. For the baseline pattern, when z = 35 mm, δ = 0.64 mm correlates to $\theta = 1°$.

In **Figure 3c**, the normalized short circuit current density, J_{sc}, is plotted versus θ. The circular symbols with error bars correspond to the system when tracking in the x-direction while the diamond symbols represent the system without tracking. This demonstrates how J_{sc} remains virtually unchanged when varying the tracking angle in contrast to the stationary system. Deviations are attributed mainly to human error of aligning the individual spring to the stage, slight misalignment of the concentrator in the spring, and imperfect reflectivity of the concentrator (issues easily mitigated by automation during array production). A misalignment between the light source angle and photodiode drops the performance more rapidly than the cosine loss, as expected for concentration optics, and can be mitigated by using lower concentrations.[39] (**Figure S6** describes analogous measurements for translation in the y-direction.)

Thermal considerations for a "unit cell" and impact on efficiency

The design of the insert for solar energy harvesting applications should be engineered to balance the concentration factor for economy of costly semiconductor material, required tolerances in alignment and tracking accuracy, and potential for excessive heating of the solar cell that would adversely impact the power conversion efficiency.[22] Focusing on heat dissipation, we expect thermal radiation and convection from the PV cell surface as well as thermal conduction by the

electrodes as illustrated in **Figure 4a**. To first order, the energy balance is governed by the Equations (2) and (3):

$$\Phi \cdot A_{conc} = \varepsilon\sigma(T_{cell}^4 - T_{air}^4) \cdot 2A_{cell} + 2\Delta T \cdot \frac{1}{R_{cool}} \cdot A_{cell} + \eta \cdot \Phi \cdot A_{conc} \quad (2)$$

$$\frac{1}{R_{cool}} = \frac{1}{R_{conv}} + \frac{1}{R_{wire}} \quad (3)$$

where Φ, A_{conc}, A_{cell}, η , ε denote the solar intensity, the area of the parabolic concentrator and solar cell, power conversion efficiency, and hemispherical emissivity, respectively. The corresponding thermal circuit diagram is shown in **Figure 4b** depicting the radiation, convection and conduction load. When the cooling resistance is equal to $10^{-1}\ K \cdot m^2/W$, the dominant dissipation methods are radiation and natural convection. As the concentration factor, CF, increases the cell temperature increases. CF is defined as the ratio A_{conc}/A_{cell}, where A_{conc} is the area of the concentrator and A_{cell} is the area of the photodiode/photovoltaic cell.

Studies have shown that power conversion efficiency drops linearly with operating cell temperature, and the temperature coefficient of GaAs is -0.08% K^{-1}.[40] This behavior is reflected in the prediction in **Figure 4c**. If the cooling resistance is reduced to 10^{-2} Km^2W^{-1}, the solar cell can maintain a lower operating temperature, as shown by the parametric curves in **Figure 4d**, and produce a higher daily accumulated energy as indicated in **Figure 4e**. An order-of-magnitude increase in CF leads to an approximately 14% drop in the daily accumulated energy value, which can be countered by an order-of-magnitude decrease in thermal resistance, physically consistent with the energy balance. The practical maximum operating temperature is determined jointly by the material selection as well as by the economics of diminishing efficiency with high CF. For instance, at $R_{cool}=10^{-3}$ Km^2W^{-1} and CF = 50 the cell temperature exceeds 42˚C, while when CF = 182 the temperature reaches 89˚C.

Shadowing effects in the kirigami tracking array

While arranging the concentrators in a hexagonal array allows a large collection area to be covered without increasing the vertical profile of the array, as with any solar tracking system, there exists a trade-off between area utilization and shadowing caused by nearby concentrators. In **Figure 5a**, *L* indicates the length of the concentrator and *W* indicates the width between concentrators. A schematic of the side view of two nearby concentrators that shadow each other are represented in **Figure 5b**. Here, *d* is the shadowed area and θ_0 is the critical angle when a shadow appears. The effective area, which is the concentrating light area, changes based on the extent of the shadowing area and when $\theta_0 < \theta < \theta_{max}$. The governing equations below assume *a* to be the side of the concentrator, A_{effect} the effective area, A_{shad} the shadowing area, and A_{total} the total area. We thus obtain:

$$A_{effect} = A_{total} - A_{shadow} \tag{4}$$

$$A_{effect} = \frac{\sqrt{3}}{2}L^2 - \frac{\sqrt{3}}{3}L \cdot [L - (L + W) \cdot cos\theta] - \frac{\sqrt{3}}{6}[L - (L + W) \cdot cos\theta]^2 \tag{5}$$

Derivations of the shadowing effect are described in the supplementary information and corresponding schematics are illustrated in **Figure S7**. Derivations of the energy density and rooftop area are further described in the supplemental information section and summarized in **Table S2**.

According to Equation (5), increasing the spacing *W* between two concentrators reduces shadowing at the expense of area utilization. **Figure 5c** illustrates this trade-off, assuming the average rooftop area is 180 m^2, CF = 182, and a fixed area for each concentrator (7.8 cm^2 if L ≈ 30 mm).[41] For a fixed panel area, increasing *W* decreases the total daily harvested energy. To avoiding shadowing, the separation distance between concentrators must increase, reducing their number (and thus, sunlight collection area) in a fixed panel area. **Figure 5d** depicts the area of semiconductor material and rooftop area needed to meet the average daily electricity requirement of 30 kWh.[42] As a benchmark, a 20%-efficient, stationary silicon panel requires 22 m^2 of semiconductor. Using higher-efficiency (e.g. 29%) GaAs semiconductor PV cells reduces the

semiconductor illuminated area requirement. This effect is multiplied by the use of the micro-concentrator arrangement, provided tracking and shadowing errors are mitigated. The latter is accomplished by increasing *W*, albeit increasing the total area occupied by the panel. Because for high efficiency PV panels the cost of semiconductor PV cells dominates the panel's bill of materials, increasing *W* is beneficial to lowering the levelized cost of electricity, as the projections below suggest.

Another design trade-off exists between the economy of semiconductor at higher CF values and increasing tracking and cell alignment precision requirements; therefore, the feasibility of lower concentration factors is considered. **Figure 6a** depicts the daily energy harvested per unit area of panel for varying CF and *W*, assuming $R_{cool} = 10^{-3}$ Km^2W^{-1}. Here, we assume the whole panel is comprised of unit cells, described as scenario 1 in **Table S2**. For a given CF, increasing *W* to reduce shadowing increases the amount of area needed to achieve the same energy output as shown in **Figure 6b**. Nevertheless, the amount of semiconductor material needed to produce the daily output requirement decreases rapidly with CF, and diminishing returns occur beyond CF > 20 (**Figure 6c**). If space is the most limiting factor for designing a tracker, minimizing *W* is the preferred approach. For example, taking the minimum *W* = 1/3L at CF = 50 (**Figure 6d**), the required area for the panel fits well within the typical available rooftop area. Only 0.246 m^2 of GaAs PV cells or 0.368 m^2 of Si PV cells are required as opposed to the total 22 m^2-area of stationary silicon PV panels needed to achieve the aforementioned daily electricity requirement. Given that the fraction of high efficiency PV panel cost attributed to the semiconductor can exceed 85%, these projected cost reductions are highly encouraging. (Comparisons between dual-axis GaAs, single-axis GaAs, stationary GaAs, and stationary Si systems are shown in **Figure S8** and more information on calculating the energy harvested for a given day is included in the supplemental information section.)

Summary and conclusions

A novel kirigami-based, multi-axis tracking mechanism and its application as a scalable solar tracking array were presented. The design parameters for achieving the desired tracking application requirements are summarized in **Figure S9**. To demonstrate tracking ability, a mini concentrator combined with a photodiode is placed within a deformed kirigami spring, and the concentrator tilts according to the displacement vector. High optical performance was maintained upon variations in the light-source angle whereby the concentrator matches the tilt angle through a corresponding lateral δ. Thermal dissipation and shadowing of nearby concentrators were calculated to influence the efficiency of solar electricity production and help guide the optimization of the concentrator and tracker design for solar-energy harvesting applications. This mechanism provides an alternative tracking method where the semiconductor consumption is an important factor and a small lateral displacement is necessary to uniformly induce tilting for a scaled array. The combination of the kirigami tracking mechanism and wide-angle microcell concentrators with high-efficiency solar cells and sufficient cooling may help enable widespread adoption of rooftop solar systems. The mechanical behavior described above enables a number of other applications, both purely mechanical in nature (e.g. a suspension or positioner design), as well as multi-functional via integration with other components and materials.

2. Experimental Section

2.1. Fabrication of tracking device

The circular kirigami patterns were fabricated by cutting polyethylene terephthalate (PET), 901 Highland Laser Printer Film (3M, 90 μm) with a 40 W Universal Laser Systems CO_2 laser cutter (5% power, 10% speed, 1000 ppi, 1.5" optics). The Young's Modulus and Poisson's ratio of the film is 2.2 GPa and 0.37, respectively. The overall diameter of the patterns was 70 mm with the largest cut radius at 27 mm.

A thin, plastic, UV-resistant, sheet is laser cut into the desired kirigami pattern, forming the kirigami base spring (**Figure 1b**). The cuts form a hexagonal shape, spacing between cuts is 1.5 mm, and two cuts along the perimeter are made. The parabolic dish concentrators are formed via vacuum-assisted thermoforming. A metal negative mold with the precise geometry to form the concentrators is perforated to allow for the vacuum thermoforming process. A thin, stiff plastic sheet of 0.5 mm thick polyethylene terephthalate glycol modified (PETG) is aligned and secured to the mold with high-temperature Kapton tape. The Vivak® PETG sheet (United States Plastic Corp)/mold are heated in an oven to 100˚C, which is above the 88˚C glass transition temperature of PETG. After the sheet/mold have uniformly reached the temperature, about ten minutes, vacuum is applied for one minute, and the mold is removed from the oven and cooled. After the sample is removed from the mold, a shadow mask is placed on the sample and 0.5 μm of silver is deposited in the wells of the parabolas via vacuum thermal evaporation (VTE). The sheet is then laser cut, yielding individual hexagonal unit cells. A top 0.1-mm thick sheet of polyethylene terephthalate (PET) is laser cut and adhered to match the geometry of the top of the concentrator with a hole for the photodiode/photovoltaic cell. A shadow mask is used to deposit electrodes on the top sheet, which is used to connect the cell. **Figure S3** shows an image of the negative mold with the plastic sheet, as well as the design of the concentrator. For this study, CF = 182 for demonstration purposes, and a rim angle of 60˚ was chosen due to surface reflections at high incident angles. More information on the design of the concentrator can be found in [22].

2.2. Mechanical testing

For mechanical testing, two rings were cut from Optically Clear Cast Acrylic Sheets (McMaster-Carr, 7/64” thick) with the laser cutter (100% power, 5% speed, 2.0” optics) to hold and align the RSK springs during tensile tests. The noise within the experimental data at lower forces is due to the resolution of the equipment and the plotted data is smoothed by adjacent averaging in OriginPro. To conduct uniaxial and shear tests, acrylic rings sandwiched the substrate and placed in holders that were 3D printed (Monoprice Maker Select, Brea, CA, USA) out of polylactic acid

(PLA). The holders were then clamped into tensile grips, and both tests were conducted at a strain rate of 1 mm/s. The force versus displacement curves were obtained via a TA.XT*Plus* Texture Analyzer (Texture Technologies, Hamilton, Massachusetts, USA) with a 30kgf load cell and the *Exponent* (Texture Technologies, Hamilton, Massachusetts, USA) software package. Work was obtained by integrating the force versus displacement data using OriginPro. Motorized lead screws attached to stages are used to translate the spring in the *x*- and *y*-directions; the CAD of the setup is shown in **Figure S10**.

2.3. Finite Element Modeling

The software package, Abaqus, was used to model the elastic behavior of the kirigami structure based on the static, general method with a 6-node linear triangular prism element (C3D6) mesh construction using the non-linear geometry option. The matrix storage is unsymmetric, full Newton method is used, and the damping factor is 0.75. Pinned boundary conditions are applied along the outermost ring and displacement conditions are applied to the innermost hexagon.

2.4. Electrical measurement

A Newport solar simulator (model# 91191-1000) is used to determine the electrical characteristics of the device, which was calibrated to AM1.5 (1000 W/m^2) using an NREL Si reference cell (model PVM233 KG5). The J-V curves are collected using an Agilent semiconductor parameter analyzer. The outermost hexagonal ring is mounted to a 3D printed holder with a cut out to allow light to penetrate. Thin, flexible copper wires connect the Si photodiode (OSRAM Opto Semiconductors, Inc., model BPW 34 S-Z) to the measurement unit. A one-axis Thorlabs motor-controlled translation stage (PT1-Z8) is mounted to the top part of the 3D printed holder. The maximum translation is 25 mm and has a resolution of 29 nm. The innermost hexagon is mounted to the stage with screws. The 3D printed holder is then mounted to a flat plate attached to a Thorlabs rotation mount (PRM1) placed over the solar simulator. There is a hole in the plate so it does not block the solar simulator. The rotational stage mimics the changes in the elevation and azimuth angle of the

sun, depending on the placement of the spring. The rotational stage tilts to the same degree as that of the spring so the concentrator remains perpendicular to the light source.

Supporting Information

Supplemental Information is available from the Wiley Online Library or from the author.

Conflict of interest

We have no financial interests to disclose.

Acknowledgments

The authors would like to thank Dr. Kyusang Lee and Dr. Aaron Lamoreaux for their help in developing the concentrator geometry. The authors would also like to thank Dr. Steve Morris and Brian Iezzi for insightful discussions. **Funding:** The authors thank the National Science Foundation grant NSF 1240264 under the Emerging Frontiers in Research and Innovation (EFRI) ODISSEI program, as well as Rackham Graduate School.

Received:

Revised:

Published online:

References

[1] T.C. Shyu, P.F. Damasceno, P.M. Dodd, A. Lamoureux, L. Xu, M. Shlian, M. Shtein, S.C. Glotzer, N.A. Kotov, *Nat. Mater*. **2015**, *14*, 785.

[2] M.K. Blees, A.W. Barnard, P.A. Rose, S.P. Roberts, K.L. McGill, P.Y. Huang, A.R. Ruyack, J.W. Kevek, B. Kobrin, D.A. Muller, P.L. McEuen, *Nat.* **2015**, *524*, 204.

[3] X. Ning, X. Wang, Y. Zhang, X. Yu, D. Choi, N. Zheng, D.S. Kim, Y. Huang, Y. Zhang, J.A. Rogers, *Adv. Mater. Int.* **2018**, *5*, 1800284.

[4] Y. Tang, Y. Li, Y. Hong, S. Yang, J. Yin, *Proc. Natl. Acad. Sci. USA* **2019**, *116*, 26407.

[5] Y. Tang, G. Lin, S. Yang, Y.K. Yi, R.D. Kamien, J. Yin, *Adv. Mater.* **2017**, *29*, 1604262.

[6] K. Gustafson, O. Angatkina, A. Wissa, *Smart Mater. Struct.* **2019**, *29*, 015013.

[7] Q. Qiao, J. Yuan, Y. Shi, X. Ning, F. Wang, *J. Mech. Robot.* **2017**, *9*.

[8] A. Rafsanjani, Y. Zhang, B. Liu, S.M. Rubinstein, K. Bertoldi, *Sci. Robot.* **2018**, *3*, eaar7555.

[9] E.E. Evke, D. Meli, M. Shtein, *Adv. Mater. Technol.* **2019**, *4*, 1900563.

[10] Y. Yamamoto, S. Harada, D. Yamamoto, W. Honda, T. Arie, S. Akita, K. Takei, *Sci. Adv.* **2016**, *2*, e1601473.

[11] S. Yao, X. Liu, S.V. Georgakopoulos, M.M. Tentzeris, in *2014 IEEE AP-S*, **2014**, 374.

[12] B.H. Kim, F. Liu, Y. Yu, H. Jang, Z. Xie, K. Li, J. Lee, J.Y. Jeong, A. Ryu, Y. Lee, D.H. Kim, X. Wang, K. Lee, J.Y. Lee, S.M. Won, N. Oh, J. Kim, J.Y. Kim, S.-J. Jeong, K.-I. Jang, S. Lee, Y. Huang, Y. Zhang, J.A. Rogers, *Adv. Funct. Mater.* **2018**, *28*, 1803149.

[13] M. Jo, S. Bae, I. Oh, J. Jeong, B. Kang, S.J. Hwang, S.S. Lee, H.J. Son, B.-M. Moon, M.J. Ko, P. Lee, *ACS Nano* **2019**, *13*, 12500.

[14] K. Zhang, Y.H. Jung, S. Mikael, J.-H. Seo, M. Kim, H. Mi, H. Zhou, Z. Xia, W. Zhou, S. Gong, Z. Ma, *Nat. Comm.* **2017**, *8*, 1.

[15] W. Wang, C. Li, H. Rodrigue, F. Yuan, M.-W. Han, M. Cho, S.-H. Ahn, *Adv. Funct. Mater.* **2017**, *27*, 1604214.

[16] L. Xu, X. Wang, Y. Kim, T.C. Shyu, J. Lyu, N.A. Kotov, *ACS Nano* **2016**, *10*, 6156.

[17] B. Roberts, M. Ghosh, P.-C. Ku, *Appl. Opt.* **2020**, *59*, 2963.

[18] Z. Liu, H. Du, J. Li, L. Lu, Z.-Y. Li, N.X. Fang, *Sci. Adv.* **2018**, *4*, eaat4436.

[19] L. Jing, Z. Wang, B. Zheng, H. Wang, Y. Yang, L. Shen, W. Yin, E. Li, H. Chen, *NPG Asia Mater* **2018**, *10*, 888.

[20] W.J. Choi, G. Cheng, Z. Huang, S. Zhang, T.B. Norris, N.A. Kotov, *Nat. Mater.* **2019**, *18*, 820.

[21] A. Lamoureux, K. Lee, M. Shlian, S.R. Forrest, M. Shtein, *Nat. Comm.* **2015**, *6*, 1.

[22] A. Lamoureux, *Thesis*, University of Michigan, **2017**.

[23] K. Lee, C.-W. Chien, B. Lee, A. Lamoureux, M. Shlian, M. Shtein, P.C. Ku, S. Forrest, *ACS Photonics* **2016**, *3*, 2134.

[24] J.F. Geisz, R.M. France, K.L. Schulte, M.A. Steiner, A.G. Norman, H.L. Guthrey, M.R. Young, T. Song, T. Moriarty, *Nat. Energy* **2020**, *5*, 326.

[25] National Renewable Energy Laboratory. **2020**. https://www.nrel.gov/pv/cell-efficiency.html, accessed: May, 2020.

[26] B. Lee, D. Fan, S.R. Forrest, *Sustain. Energy Fuels* **2020**, 10.1039.C9SE01255A.

[27] C.-Y. Lee, P.-C. Chou, C.-M. Chiang, C.-F. Lin, *Sensors (Basel)* **2009**, *9*, 3875.

[28] W. Nsengiyumva, S.G. Chen, L. Hu, X. Chen, *Renew. Sust. Energ. Rev.* **2018**, *81*, 250.

[29] F. Duerr, Y. Meuret, H. Thienpont, *Opt. Express.* **2011**, *19*, A207.

[30] A.J. Grede, J.S. Price, N.C. Giebink, *Opt. Express.* **2016**, *24*, A1635.

[31] J.S. Price, X. Sheng, B.M. Meulblok, J.A. Rogers, N.C. Giebink, *Nat. Comm.* **2015**, *6*, 1.

[32] H. Apostoleris, M. Stefancich, M. Chiesa, *Nat. Energ.* **2016**, *1*, 1.

[33] S.A. Zirbel, R.J. Lang, M.W. Thomson, D.A. Sigel, P.E. Walkemeyer, B.P. Trease, S.P. Magleby, L.L. Howell, *J. Mech. Des.* **2013**, *135*.

[34] Y. Chen, Y. Lu, M. Liao, Y. Tian, Q. Liu, C. Gao, X. Yang, C. Shan, *Adv. Funct. Mater.* **2019**, *29*, 1906040.

[35] C.-H. Lin, D.-S. Tsai, T.-C. Wei, D.-H. Lien, J.-J. Ke, C.-H. Su, J.-Y. Sun, Y.-C. Liao, J.-H. He, *ACS Nano.* **2017**, *11*, 10230.

[36] Chih-Wei Chien, Kyusang Lee, M. Shlian, S. Forrest, M. Shtein, P.C. Ku, in *2015 IEEE 42nd PVSC*. **2015**, 1.

[37] L. Lisell, T. Tetreault, A. Watson, *Solar Ready Buildings Planning Guide*, **2009**.

[38] D.G. Hwang, M.D. Bartlett, *Sci. Rep.* **2018**, *8*, 1.

[39] N. Sellami, T.K. Mallick, *Appl. Energ.* **2013**, *102*, 868.

[40] T.J. Silverman, M.G. Deceglie, B. Marion, S. Cowley, B. Kayes, S. Kurtz, in *2013 IEEE 39th PVSC*. **2013**, 0103.

[41] P. Gagnon, R. Margolis, J. Melius, C. Phillips, R. Elmore, *National Renewable Energy Laboratory*, Golden, CO. **2016**.

[42] *Residential Energy Consumption Survey: Electric Sales, Revenue, and Average Price, Table 5.a*, U.S. Energy Information Administration. **2019**.

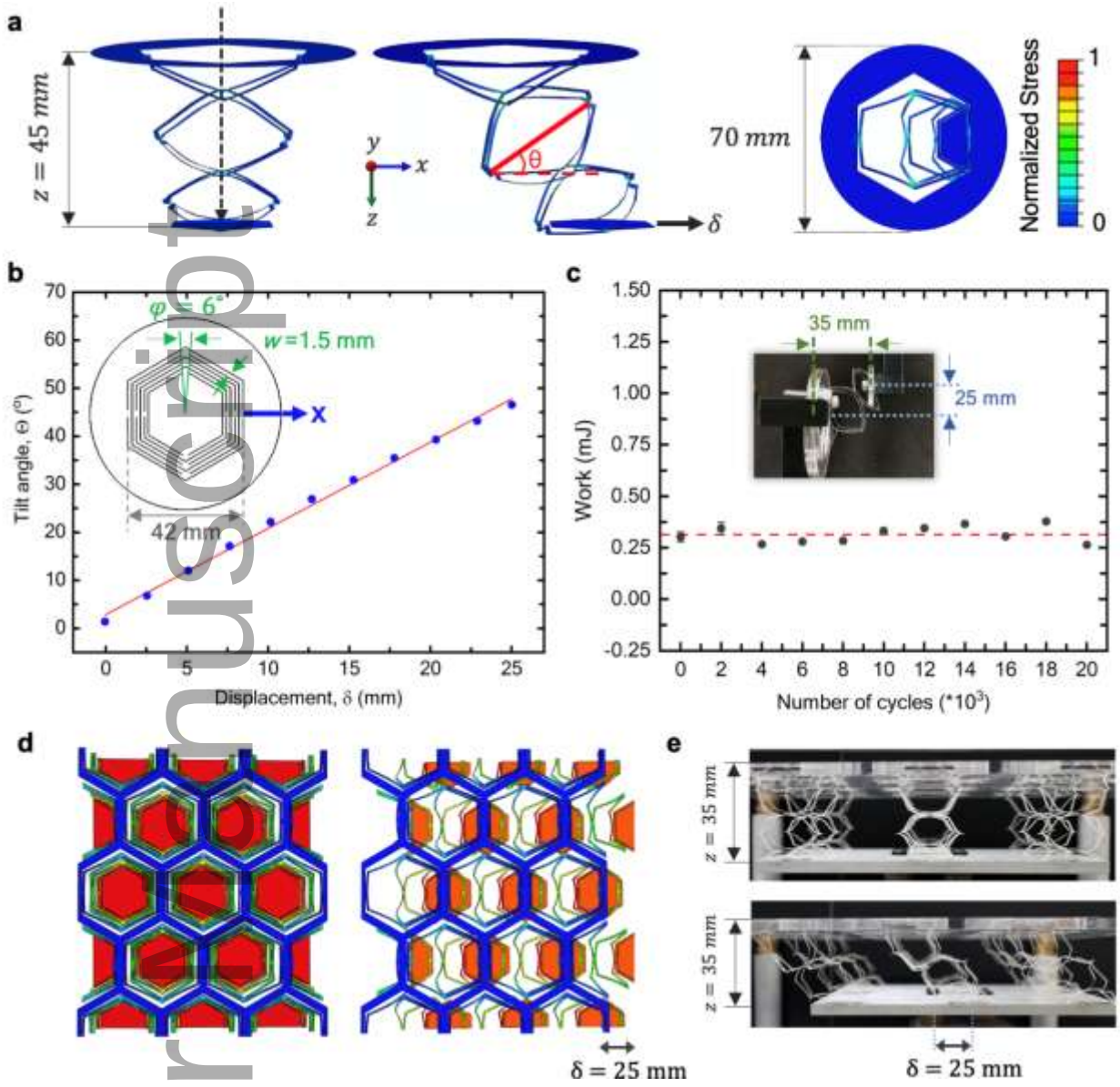

Figure 1. Tilting mechanism of a hexagonal kirigami spring. a) Left: side view of FE model of a deformed spring displaced 45 mm in the z-direction, middle: side view and right: top view of model displaced 25 mm in the *x*-direction and 45 mm in the *z*-direction; color bar indicates normalized stress. b) Experimental measurement of tilt angle based on displacement in the *x*-direction maintaining a height of 35 mm with linear fit where w = 1.5 mm and $\varphi = 6^{\circ}$. c) Work required to shear the spring in the *x*-direction by 25 mm for up to 10,000 cycles, maintaining a height of 35 mm. d) FE model of deformed array arranged in a honeycomb pattern in the *x*-direction at $\delta = 0\ mm$ (left) and $\delta = 25\ mm$ (right) where $z = 35\ mm$. e) Side view of deformed physical array arranged in a rectangular pattern for visual clarity at $\delta = 0\ mm$ (top) and $\delta = 25\ mm$ (bottom) in the *x*-direction where $z = 35\ mm$.

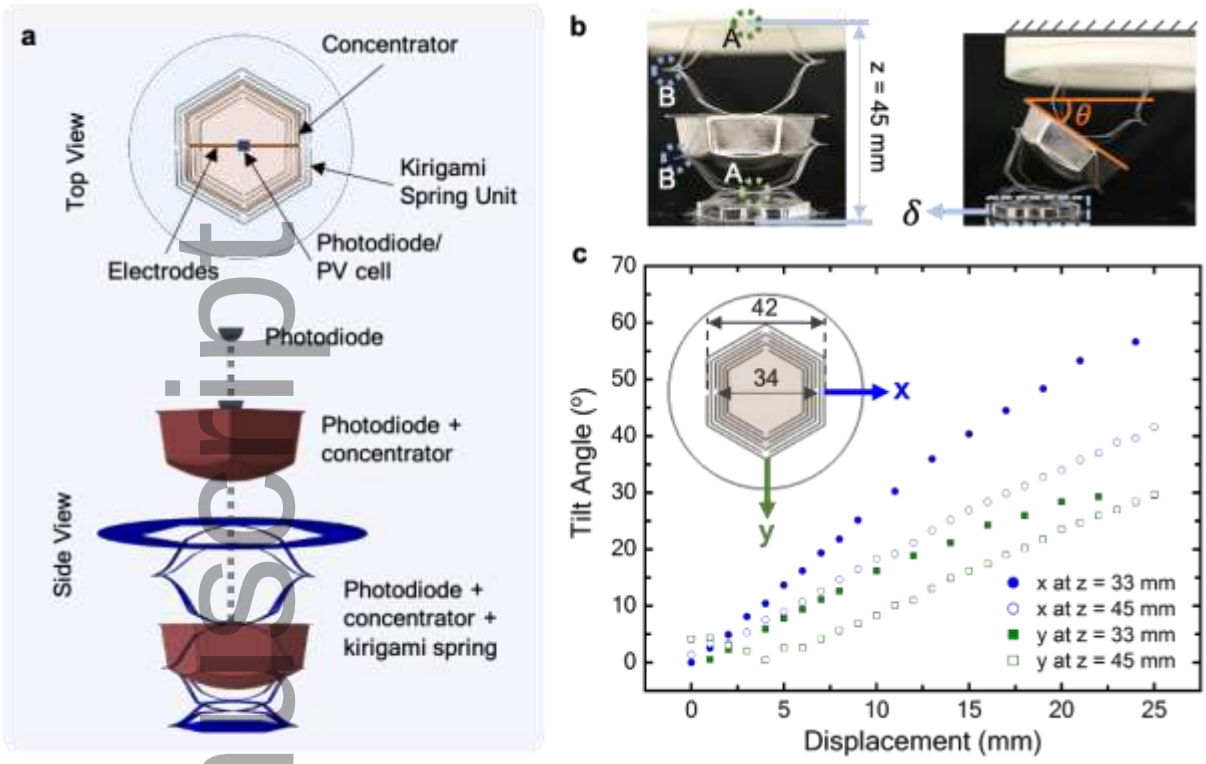

Figure 2. Tilting mechanism of a kirigami hexagonal spring with concentrators embedded in the middle ring. a) Top view and side view of the tracker with kirigami cut pattern and locations of the concentrator, photodiode or photovoltaic cell, and electrodes. b) Images of kirigami spring deformed at z = 45 mm with concentrator placed in middle ring (left) and displaced δ = 25 mm in the y-direction, prompting the concentrator to tilt $\theta = 37°$ (right). A and B represent pivot points at the edge and corner of the pattern, respectively. c) Experimental measurements of the tracker displaced in the x- or y-direction at deformed lengths of 33 and 45 mm. Inset represents cut pattern.

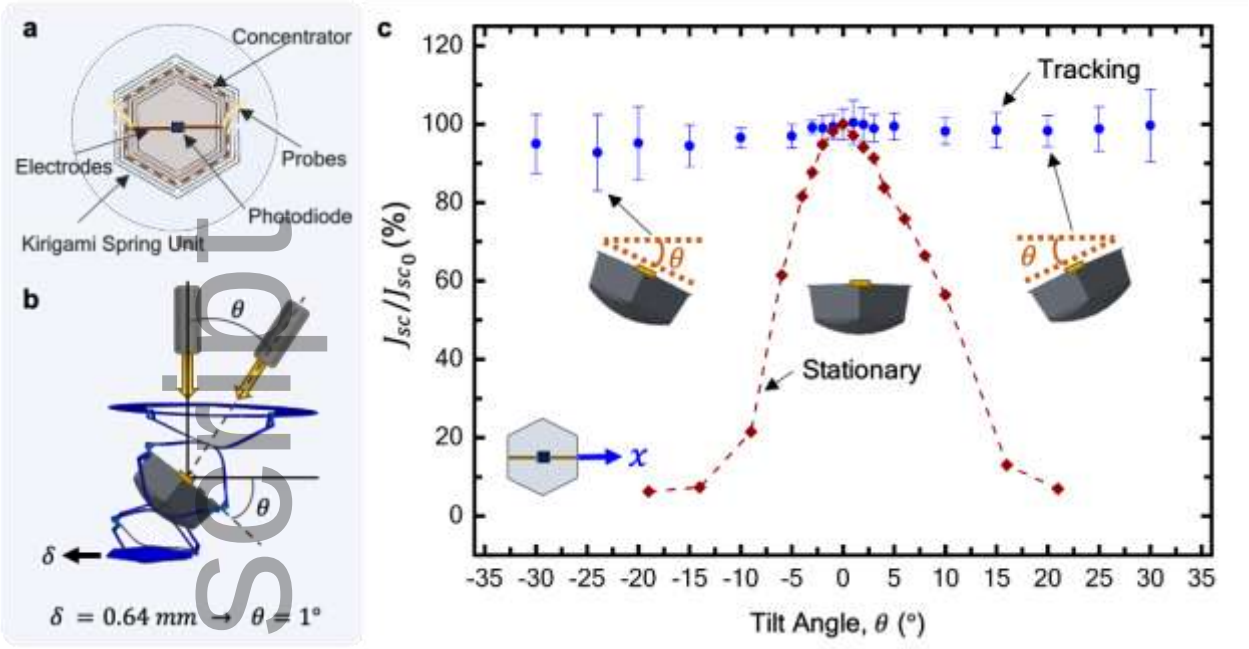

Figure 3. Tracking performance of the kirigami spring integrated with mini concentrators in *x*-direction. a) Top view of tracker, depicting cut pattern of kirigami spring; the concentrator, photodiode, and electrodes locations; and placement of probes for measuring the electrical current. b) Side view of electrical measurement setup, in which the spring tilts to maintain its position with the light source at various angles. c) Experimental measurements of the short circuit current to the initial short circuit current at various tilt angles of the tracker and stationary systems. Blue circles with error bars represent tracking system, and red diamonds represent stationary system with schematics represent $\theta = 0°$ and $\theta = \pm 22°$.

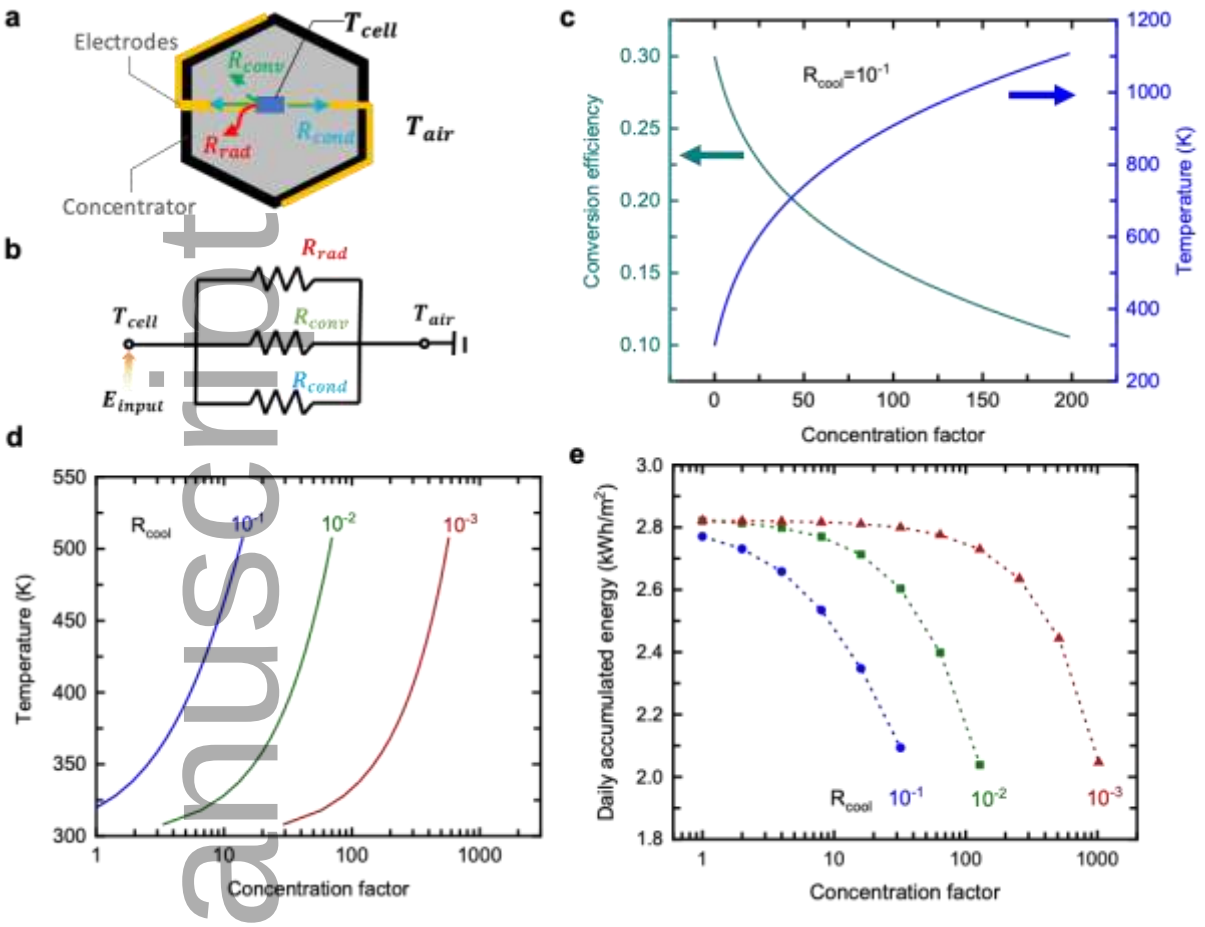

Figure 4. Theoretical thermal effects of the cell on conversion efficiency and energy. a) Schematic illustration of the types of heat dissipation in the solar cell. b) Respective thermal circuit diagram with radiation, convection and conduction load. c) Temperature and efficiency as a function of concentration factor where $R_{cool} = 10^{-1}\ K \cdot m^2/W$. d) Temperature and e) daily accumulated energy versus logarithmic CF with cooling resistance equal to 10^{-1}, 10^{-2}, $10^{-3} K \cdot m^2/W$.

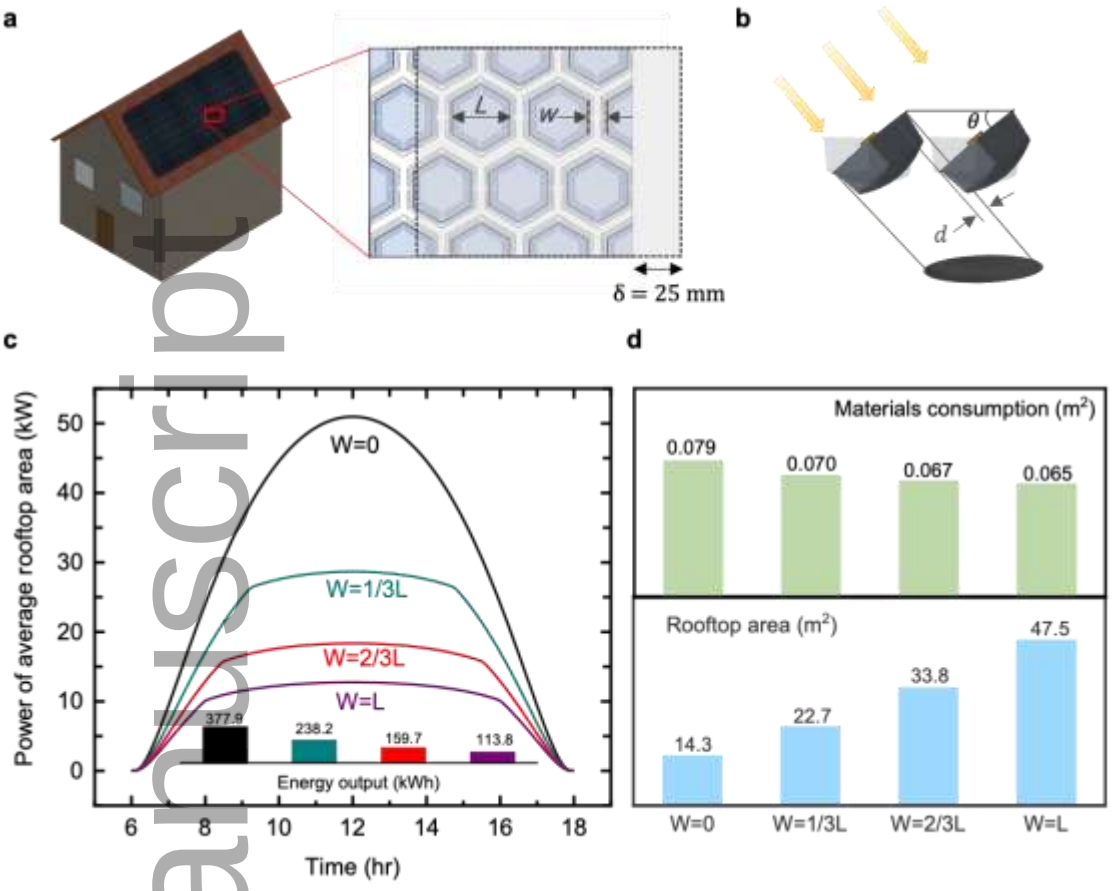

Figure 5. Effect of shadowing on the performance of solar trackers. a) Schematic of solar array on the roof of a house and close-up of the cut pattern array with shaded area representing the area extent of displacing the tracker by 25 mm; L represents the length and W represents the width between concentrators. b) Side view of packed neighbor concentrators, where θ is the tilt angle and d is the shadowing area. c) Total instantaneous power output produced by average 180 m^2 rooftop area versus time of a day. Assuming 30% conversion efficiency and cooling resistance equal to $10^{-3}\ K \cdot m^2/W$. Inset: energy accumulated over the day. d) Comparison of materials consumption and rooftop area needed to meet daily energy requirement at CF = 182 with different W, assuming daily energy requirement equal to 30 kWh.

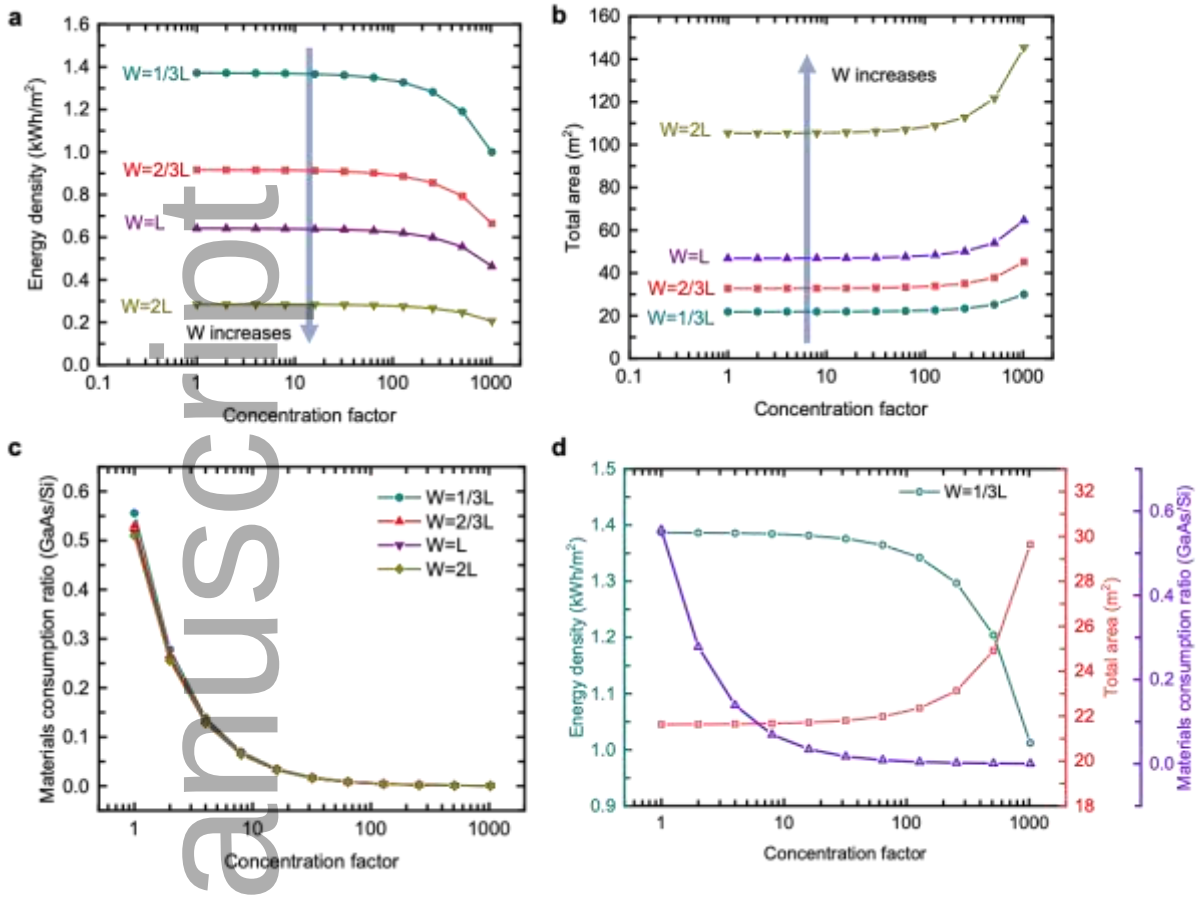

Figure 6. Shadowing of concentrators and cell temperature influences on energy density, area, and cost, having a maximum tilt angle $\theta = 55°$. a) Energy density as a function of CF with varying W. b) Total rooftop area and c) materials consumption ratio needed to meet daily average energy requirement. d) Comparison of energy density, required rooftop area, and materials consumption ratio as a function of CF when $W = L$.